Incomplete immunity to backscattering in chiral one-way photonic crystals

Pi-Ju Cheng,[1,2] **Chung-Hao Tien,**[2] **and Shu-Wei Chang**[1,2,*]

[1] *Research Center for Applied Sciences, Academia Sinica, Nankang, Taipei 11529, Taiwan*
[2] *Department of Photonics, National Chiao-Tung University, Hsinchu 30010, Taiwan*

[*] *swchang@sinica.edu.tw*

Abstract: We show that the propagating modes in a strongly-guided chiral one-way photonic crystal are not backscattering-immune even though they are indeed insensitive to many kinds of scatters. Since these modes are not protected by the nonreciprocity, the backscattering does occur under certain circumstances. We use a perturbative method to derive criteria for the prominent backscattering in such chiral structures. From both our theory and numerical examinations, we find that the amount of backscattering critically depends on the symmetry of scatters. Additionally, for these chiral photonic modes, disturbances at the most intense parts of field profiles do not necessarily lead to the most effective backscattering.

OCIS codes: (230.5298) Photonic crystals; (290.1350) Backscattering; (290.5855) Scattering, polarization.

References and links

1. D. Jalas, A. Petrov, M. Eich, W. Freude, S. Fan, Z. Yu, R. Baets, M. Popovic, A. Melloni, J. D. Joannopoulos, M. Vanwolleghem, C. R. Doerr, and H. Renner, "What is–and what is not–an optical isolator," Nat. Photonics **7**, 579–582 (2013).
2. K. v. Klitzing, G. Dorda, and M. Pepper, "New method for high-accuracy determination of the fine-structure constant based on quantized Hall resistance," Phys. Rev. Lett. **45**, 494–497 (1980).
3. B. I. Halperin, "Quantized Hall conductance, current-carrying edge states, and the existence of extended states in a two-dimensional disordered potential," Phys. Rev. B **25**, 2185–2190 (1982).
4. X. G. Wen, "Gapless boundary excitations in the quantum Hall states and in the chiral spin states," Phys. Rev. B **43**, 11025–11036 (1991).
5. F. D. M. Haldane and S. Raghu, "Possible realization of directional optical waveguides in photonic crystals with broken time-reversal symmetry," Phys. Rev. Lett. **100**, 013904 (2008).
6. Z. Wang, Y. D. Chong, J. D. Joannopoulos, and M. Soljačić, "Reflection-free one-way edge modes in a gyromagnetic photonic crystal," Phys. Rev. Lett. **100**, 013905 (2008).
7. S. Raghu and F. D. M. Haldane, "Analogs of quantum-Hall-effect edge states in photonic crystals," Phys. Rev. A **78**, 033834 (2008).
8. Z. Wang, Y. Chong, J. D. Joannopoulos, and M. Soljačić, "Observation of unidirectional backscattering-immune topological electromagnetic states," Nature **461**, 772–775 (2009).
9. X. Ao, Z. Lin, and C. T. Chan, "One-way edge mode in a magneto-optical honeycomb photonic crystal," Phys. Rev. B **80**, 033105 (2009).
10. J.-X. Fu, R.-J. Liu, and Z.-Y. Li, "Robust one-way modes in gyromagnetic photonic crystal waveguides with different interfaces," Appl. Phys. Lett. **97**, 041112 (2010).
11. Y. Poo, R.-x. Wu, Z. Lin, Y. Yang, and C. T. Chan, "Experimental realization of self-guiding unidirectional electromagnetic edge states," Phys. Rev. Lett. **106**, 093903 (2011).
12. K. Fang, Z. Yu, and S. Fan, "Microscopic theory of photonic one-way edge mode," Phys. Rev. B **84**, 075477 (2011).
13. K. Fang, Z. Yu, and S. Fan, "Realizing effective magnetic field for photons by controlling the phase of dynamic modulation," Nat. Photonics **6**, 782–787 (2012).

#230637 - $15.00 USD Received 12 Dec 2014; revised 2 Apr 2015; accepted 6 Apr 2015; published 14 Apr 2015

14. K. Fang and S. Fan, "Controlling the flow of light using the inhomogeneous effective gauge field that emerges from dynamic modulation," Phys. Rev. Lett. **111**, 203901 (2013).
15. M. C. Rechtsman, J. M. Zeuner, Y. Plotnik, Y. Lumer, D. Podolsky, F. Dreisow, S. Nolte, M. Segev, and A. Szameit, "Photonic Floquet topological insulators," Nature **496**, 196–200 (2013).
16. A. E. Serebryannikov and E. Ozbay, "Isolation and one-way effects in diffraction on dielectric gratings with plasmonic inserts," Opt. Express **17**, 278–292 (2009).
17. A. E. Serebryannikov and E. Ozbay, "Unidirectional transmission in non-symmetric gratings containing metallic layers," Opt. Express **17**, 13335–13345 (2009).
18. W.-M. Ye, X.-D. Yuan, C.-C. Guo, and C. Zen, "Unidirectional transmission in non-symmetric gratings made of isotropic material," Opt. Express **18**, 7590–7595 (2010).
19. S. W. Chang, "Bidirectionality in bianistropic but reciprocal photonic crystals and its usage in active photonics," J. Lightwave Technol. **32**, 10–19 (2014).
20. A. B. Khanikaev, S. H. Mousavi, W.-K. Tse, M. Kargarian, A. H. MacDonald, and G. Shvets, "Photonic topological insulators," Nat. Mater. **12**, 233–239 (2013).
21. O. Pankratov, S. Pakhomov, and B. Volkov, "Supersymmetry in heterojunctions: band-inverting contact on the basis of $\mathrm{Pb}_{1-x}\mathrm{Sn}_x\mathrm{Te}$ and $\mathrm{Hg}_{1-x}\mathrm{Cd}_x\mathrm{Te}$," Solid State Commun. **61**, 93–96 (1987).
22. C. L. Kane and E. J. Mele, "Z_2 topological order and the quantum spin Hall effect," Phys. Rev. Lett. **95**, 146802 (2005).
23. B. A. Bernevig, T. L. Hughes, and S.-C. Zhang, "Quantum spin Hall effect and topological phase transition in HgTe quantum wells," Science **314**, 1757–1761 (2006).
24. L. Fu and C. L. Kane, "Topological insulators with inversion symmetry," Phys. Rev. B **76**, 045302 (2007).
25. M. Z. Hasan and C. L. Kane, "Colloquium: topological insulators," Rev. Mod. Phys. **82**, 3045–3067 (2010).
26. H. Cory, "Chiral devices-an overview of canonical problems," J. Electromagnet Wave **9**, 805–829 (1995).
27. G. Shvets, "Optical polarizer/isolator based on a rectangular waveguide with helical grooves," Appl. Phys. Lett. **89**, 141127 (2006).
28. M. Thiel, M. Decker, M. Deubel, M. Wegener, S. Linden, and G. von Freymann, "Polarization stop bands in chiral polymeric three-dimensional photonic crystals," Adv. Mater. **19**, 207–210 (2007).
29. V. I. Kopp, V. M. Churikov, G. Zhang, J. Singer, C. W. Draper, N. Chao, D. Neugroschl, and A. Z. Genack, "Single- and double-helix chiral fiber sensors," J. Opt. Soc. Am. B **24**, A48–A52 (2007).
30. S. Gennady, T. Simeon, I. K. Victor, N. Daniel, and Z. G. Azriel, "Polarization properties of chiral fiber gratings," J. Opt. A: Pure Appl. Opt. **11**, 074007 (2009).
31. W.-J. Chen, Z. H. Hang, J.-W. Dong, X. Xiao, H.-Z. Wang, and C. T. Chan, "Observation of backscattering-immune chiral electromagnetic modes without time reversal breaking," Phys. Rev. Lett. **107**, 023901 (2011).
32. L. Zhang, W. He, K. Ronald, A. Phelps, C. Whyte, C. Robertson, A. Young, C. Donaldson, and A. Cross, "Multimode coupling wave theory for helically corrugated waveguide," IEEE Trans. Microwave Theory Tech. **60**, 1–7 (2012).
33. J. A. Kong, *Electromagnetic Wave Theory*, last ed. (EMW Publishing, 2008).
34. J. J. Sakurai, *Modern Quantum Mechanics*, revised ed. (Addison Wesley, 1994).
35. S. L. Chuang, "A coupled mode formulation by reciprocity and a variational principle," J. Lightwave Technol. **5**, 5–15 (1987).

---

1. Introduction

The reduction of unwanted reflections and backscattering during wave transmissions and propagations is important in photonic integrated systems. It lowers potential channel noises and interferences and therefore necessitates the device *isolator* [1]. Such devices only transmit the optical power along one direction but block the energy flow in the other. To implement this functionality in a robust manner, nonreciprocal setups are required. In electronics, the one-way phenomenon is present in the edge states of quantum Hall effect due to a high magnetic field that breaks the time-reversal symmetry [2–4]. Analogously, in photonics, unidirectional edge modes can be also implemented using photonic crystals (PhCs) with static magneto-optical effects [5–12] or dynamic phase modulations (including spatially-equivalent ones) [13–15].

Despite various nonreciprocal schemes aimed at one-way behaviors of waves, their compatibilities with photonic systems nowadays still require some key progress. Since most of the conventional linear optical devices are reciprocal, great efforts have to be devoted to the integrations of nonreciprocal (magnetic) materials or complicated time-variant controls to photonic structures. These inconveniences motivate the development of reciprocal schemes which distinguish or isolate energy flows in opposite directions. For example, asymmetric two-way transmissions may be achieved through designed gratings [16–18]. In wave-guiding structures, reciprocal modes that are backscattering-immune to a variety of scatters are preferred so that energy flows are not easily reversed. This, however, does not mean only unidirectional modes are supported. In fact, in reciprocal environments, counter-propagating modes always exist simultaneously, namely, a reciprocal photonic system is bidirectional [19].

Two factors are essential to the immunity of modes (states) to backscattering in reciprocal (time-reversible) systems. As long as (i) the counter-propagating modes (states) are firmly associated with some orthogonal degrees of freedom (DOFs), and (ii) elastic scatters do not mix these DOFs, the backscattering is suppressed. Such characteristics can be found in the edge modes (states) of photonic (electronic) topological insulators [20–25]. In fact, these prerequisites on one-way propagations are also present in circularly-polarized (CP) guided modes of one-dimensional (1D) chiral PhCs or waveguides (WGs) [26–32]. In this case, the key DOFs are the two circular polarizations rotating in opposite orientations. Absence of the backscattering from simple scatters has also been demonstrated experimentally in 1D chiral PhCs [31].

While the aforementioned condition (ii) may hold for a broad range of scatters, there are always exceptions. The failure of this condition marks the onset of backscattering. This point motivates us to examine the robustness of reciprocal chiral guided modes against the backscattering. In this work, we look into the dependencies of backscattering on geometries of different scatters in a 1D chiral PhC covered by perfect electric conductors (PECs) at microwave frequencies. We use the first-order Born approximation and coupled-mode theory to develop the criteria of prominent scattering in the chiral structure. The outcomes indicate that the amount of backscattering closely depends on the cross-sectional symmetry of scatters. In addition, even if the scatter is placed at positions corresponding to the most intense parts of mode profiles, the backscattering there is not necessarily the most prominent. The behavior is contrary to that of typical backscattering in generic PEC WGs. All these features are qualitatively verified by rigorous numerical calculations. Our studies also point out what types of scatters or defects should be avoided in one-way applications of chiral structures so that the backscattering could be minimized. While this work is aimed at microwave frequencies, the results may be generalized to analogous plasmonic chiral PhCs at optical frequencies after the structure size and operating wavelength are properly scaled down.

The rest of this paper is organized as follows. In section 2, the structure and modes of the 1D chiral PhC as well as the setup of backscattering will be briefly introduced. The theoretical model based on coupled-mode theory are outlined in section 3. In section 4, we will discuss the inferences from our theory on backscattering and present the numerical results and their comparisons with theoretical predictions. The conclusion will be given in section 5.

2. Structure of chiral one-way photonic cyrstal

The schematic diagram of the 1D chiral PhC in this study is shown in Fig. 1. This chiral structure is generalized from a circular PEC WG with its radius $R = 1$ cm and center coincident with the z axis. The interior of the PhC is filled with air and has a relative permittivity of unity. A generic cross section of the PhC is shown in the top inset of the same figure. A PEC bump in the form of a truncated sector is present at the circular rim of the cross section. The thickness ΔR and outer arc length ΔS of the bump are $0.15R$ and $0.3R$, respectively. The chiral PhC is a right-handed (RH) structure and has a pitch P. Since its cross section does not have any symmetries, the pitch P is also the period of this PhC. The bottom inset of Fig. 1 shows a scatter to be inserted into the PhC. We focus on chiral scatters with a pitch P_s and cross sections of different rotational symmetries. As will be shown later, chiral scatters reflect the propagating modes effectively even though other types of scatters could also result in backscattering.

In absence of the bump, eigenmodes of the circular PEC WG are analytically solvable [33].

Received 12 Dec 2014; revised 2 Apr 2015; accepted 6 Apr 2015; published 14 Apr 2015

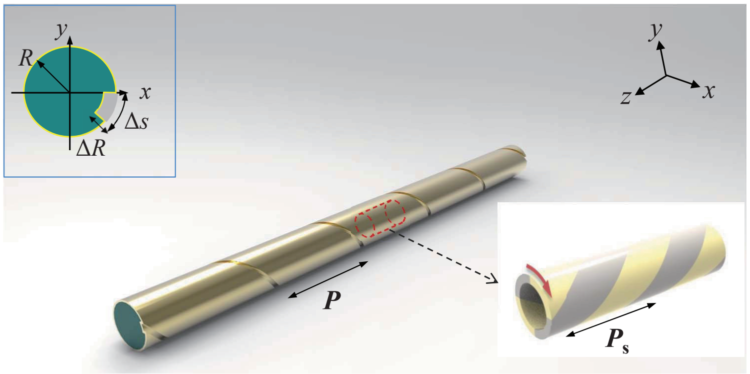

Fig. 1. The schematic diagram of the one-way chiral PhC covered by PECs. The top inset shows a generic cross section inside the PhC. The bottom inset indicates a chiral scatter to be inserted into the the wave-guiding structure.

They can be divided into transverse-electric (TE) modes TE_{mn} and transverse-magnetic (TM) modes TM_{mn}, where $m \in \mathbb{Z}$ and $n \geq 1$ are the azimuthal and radial mode numbers, respectively. Hereafter, we adopt the representation $\exp(im\phi)/\sqrt{2\pi}$ for azimuthal parts of various cylindrical field components, where ϕ is the azimuthal angle. The fundamental modes are two degenerate TE modes $\mathrm{TE}_{\pm1,1}$. These two modes are of interest since their polarization patterns resemble circular polarizations and can properly grasp features of the chirality. With optic conventions for waves propagating toward the $+\hat{z}$ direction, the $\mathrm{TE}_{+1,1}$ and $\mathrm{TE}_{-1,1}$ modes are similar to the left-handed circularly-polarized (LHCP) and right-handed circularly-polarized (RHCP) waves with polarizations $\hat{e}_+ = (\hat{x} + i\hat{y})/\sqrt{2}$ and $\hat{e}_- = \hat{e}_+^*$, respectively. On the other hand, upon reversing the propagation toward the $-\hat{z}$ direction, the LHCP and RHCP waves change their polarizations into $\hat{e}_-$ and $\hat{e}_+$ and are therefore associated with $\mathrm{TE}_{-1,1}$ and $\mathrm{TE}_{+1,1}$ modes, respectively.

To make the chiral nature of backscattering clear, we attempt to rule out the characteristics of higher-order modes other than $\mathrm{TE}_{\pm1,1}$ ones in this process. Therefore, we adopt the frequency range below which the next guided mode $\mathrm{TM}_{0,1}$ and other even higher-order modes are all cut off. Accordingly, the pitch P is set to 6 cm so that the chiral bandgap responsible for one-way propagations is opened between the cutoff frequencies of $\mathrm{TE}_{\pm1,1}$ and $\mathrm{TM}_{0,1}$ modes. Figure 2(a) shows bandstructures of the chiral PhC around the frequency range of interest in the first Brillouin zone (BZ) for wave number $k_z \geq 0$. The calculations are carried out with the eigenfrequency solver of commercial software COMSOL. A phase difference $\exp(ik_zP)$ is imposed on the fields at two sides of the unit cell to setup the boundary condition of Bloch modes. The dispersion curves of $\mathrm{TE}_{\pm1,1}$ modes are also shown in the scheme of reduced zones for comparisons. The chiral bump breaks the degeneracy of $\mathrm{TE}_{\pm1,1}$ modes and turn them into the LHCP-like and RHCP-like modes. While the dispersion curve of LHCP-like modes is only slightly shifted in frequencies as compared to that of $\mathrm{TE}_{\pm1,1}$ modes, an additional chiral bandgap from 9.90 to 10.42 GHz is developed on the counterpart of RHCP-like modes at the BZ center due to the RH chiral structure. In the frequency range of this chiral bandgap, only LHCP-like modes can propagate while RHCP-like ones behave like evanescent waves. Since the forward- and backward-propagating LHCP-like modes have distinct polarizations patterns similar to $\hat{e}_+$ and $\hat{e}_-$, respectively, the two waves would simply pass by those scatters which cannot mix polarizations $\hat{e}_\pm$ and hence are not effectively reflected.

As a test of the similarity between the $\mathrm{TE}_{+1,1}$ and forward-propagating LHCP-like modes, we monitor the incidence of the $\mathrm{TE}_{+1,1}$ mode from the circular WG to the chiral PhC at a frequency of 10.25 GHz within the chiral bandgap, which is also the frequency of LHCP-like modes at the

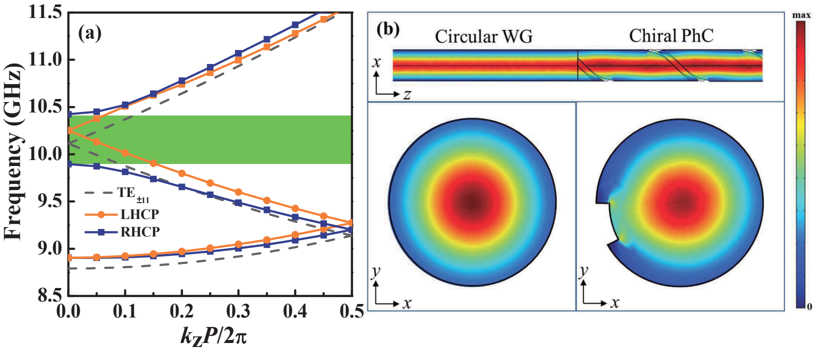

Fig. 2. (a) Bandstructures of the 1D chiral PhC. The dispersion curves of unperturbed $\mathrm{TE}_{\pm1,1}$ modes are split into those of the LHCP-like and RHCP-like modes. The RHCP-like mode has a chiral bandgap at the BZ center. (b) The incidence of a forward-propagating $\mathrm{TE}_{+1,1}$ mode from the circular WG into chiral PhC. The cross-sectional distributions of square field magnitudes in the WG and PhC regions are shown at the bottom. Except for areas near the bump, the two field patterns look similar.

BZ center. The cross-sectional view of the field pattern near the junction of the WG and PhC is illustrated in Fig. 2(b). Only minor reflections and field variations due to the discontinuity of the wave-guiding structure are observed. As shown at the bottom of Fig. 2(b), the cross-sectional distributions of field strengths in the WG and PhC regions are similar except for areas near the bump. This examination confirms the resemblance between the $\mathrm{TE}_{+1,1}$ mode of the circular WG and forward-propagating LHCP-like mode of the chiral PhC. Since no significant reflections are observed here, this incidence scheme will also be utilized in later calculations to excite the forward-propagating LHCP-like mode inside the chiral PhC.

3. Theoretical model of backscattering

We use a perturbative scheme to investigate the backscattering in chiral structures. While the chiral PEC bump in Fig. 1 and some scatters to be considered are not really weak perturbations, the derivation here does provide some insights into the backscattering in this chiral PhC. In sections 3.1 and 3.2, we briefly describe some preliminary knowledge on the modeling. Details about the backscattering are presented in sections 3.3.

3.1. Scatters as effective radiation sources: first-order Born approximation

In the presence of a scatter, the total field $\mathbf{E}(\mathbf{r})$ in a chiral PhC, of which the permittivity profile is slightly different from that of a circular PEC WG, satisfies the following wave equation:

$$\begin{aligned}&\nabla\times\nabla\times\mathbf{E}(\mathbf{r})-\left(\frac{\omega}{c}\right)^2\varepsilon_{\mathrm{r}}(\mathbf{r},\omega)\mathbf{E}(\mathbf{r})=\mathbf{0},\ \ \forall\ \ 0<\rho<R,\\&\varepsilon_{\mathrm{r}}(\mathbf{r},\omega)=\Delta\varepsilon_{\mathrm{r,s}}(\mathbf{r},\omega)+\varepsilon_{\mathrm{r,c}}(\mathbf{r},\omega),\ \ \varepsilon_{\mathrm{r,c}}(\mathbf{r},\omega)=\Delta\varepsilon_{\mathrm{r,c}}(\mathbf{r},\omega)+\varepsilon_{\mathrm{r,b}}(\omega),\end{aligned}\tag{1}$$

where ω is the angular frequency of the field; c is the speed of light in the vacuum; $\rho=|\boldsymbol{\rho}|$ is the magnitude of the transverse coordinate ($\boldsymbol{\rho}=x\hat{x}+y\hat{y}$); $\varepsilon_{\mathrm{r}}(\mathbf{r},\omega)$ is the overall relative permittivity distribution inside the chiral PhC; $\Delta\varepsilon_{\mathrm{r,s}}(\mathbf{r},\omega)$ is the permittivity variation due to the scatter; and $\varepsilon_{\mathrm{r,c}}(\mathbf{r},\omega)$ is the permittivity profile of the chiral PhC, which includes a chiral component $\Delta\varepsilon_{\mathrm{r,c}}(\mathbf{r},\omega)$ and uniform background $\varepsilon_{\mathrm{r,b}}(\omega)$ (set to unity). The total field $\mathbf{E}(\mathbf{r})=\mathbf{E}_{\mathrm{i}}(\mathbf{r})+\mathbf{E}_{\mathrm{s}}(\mathbf{r})$ is composed of an incident field $\mathbf{E}_{\mathrm{i}}(\mathbf{r})$ and scattered part $\mathbf{E}_{\mathrm{s}}(\mathbf{r})$. The field $\mathbf{E}_{\mathrm{s}}(\mathbf{r})$ is induced by

#230637 - $15.00 USD Received 12 Dec 2014; revised 2 Apr 2015; accepted 6 Apr 2015; published 14 Apr 2015

the scatter and is our target. If the scatter is a mild one, we may use the perturbation theory [in the order of $\Delta\varepsilon_{\mathrm{r,s}}(\mathbf{r},\omega)$] to approximate the governing equation of $\mathbf{E}_{\mathrm{s}}(\mathbf{r})$.

The zeroth-order equation is the wave equation of $\mathbf{E}_{\mathrm{i}}(\mathbf{r})$ in the scatter-free chiral PhC. Along with the first-order equation of $\mathbf{E}_{\mathrm{s}}(\mathbf{r})$, they are shown as follows:

$$\nabla\times\nabla\times\mathbf{E}_{\mathrm{i}}(\mathbf{r})-\left(\frac{\omega}{c}\right)^2\varepsilon_{\mathrm{r,c}}(\mathbf{r},\omega)\mathbf{E}_{\mathrm{i}}(\mathbf{r})=\mathbf{0}. \tag{2a}$$

$$\nabla\times\nabla\times\mathbf{E}_{\mathrm{s}}(\mathbf{r})-\left(\frac{\omega}{c}\right)^2\varepsilon_{\mathrm{r,c}}(\mathbf{r},\omega)\mathbf{E}_{\mathrm{s}}(\mathbf{r})\approx i\omega\mu_0\mathbf{J}_{\mathrm{s}}(\mathbf{r}),\;\; \mathbf{J}_{\mathrm{s}}(\mathbf{r})\equiv -i\omega\varepsilon_0\Delta\varepsilon_{\mathrm{r,s}}(\mathbf{r},\omega)\mathbf{E}_{\mathrm{i}}(\mathbf{r}), \tag{2b}$$

where $\mathbf{J}_{\mathrm{s}}(\mathbf{r})$ is an effective source resulted from the coupling between $\mathbf{E}_{\mathrm{i}}(\mathbf{r})$ and $\Delta\varepsilon_{\mathrm{r,s}}(\mathbf{r},\omega)$. Equation (2b) indicates that the scattered field $\mathbf{E}_{\mathrm{s}}(\mathbf{r})$ could be regarded as being radiated from the source $\mathbf{J}_{\mathrm{s}}(\mathbf{r})$ in the chiral PhC. Such a simplification is analogous to the first-order Born approximation in quantum mechanics [34]. It turns the full calculation of $\mathbf{E}(\mathbf{r})$ into an effective radiation problem, which could be further analyzed through mode expansions later.

3.2. Generalized reciprocity theorem in waveguide-like structures and mode orthogonality

Let us consider two sets of electric and magnetic fields $[\mathbf{E}_1(\mathbf{r}),\mathbf{H}_1(\mathbf{r})]$ and $[\mathbf{E}_2(\mathbf{r}),\mathbf{H}_2(\mathbf{r})]$ which are independently generated by two sources $\mathbf{J}_1(\mathbf{r})$ and $\mathbf{J}_2(\mathbf{r})$ at a frequency ω in two different WG-like structures 1 and 2 extending along the z axis, respectively. The permittivity distributions of structures 1 and 2 are denoted as $\varepsilon_{\mathrm{r},1}(\mathbf{r},\omega)$ and $\varepsilon_{\mathrm{r},2}(\mathbf{r},\omega)$, and their relative permeabilities $\mu_{\mathrm{r},1}$ and $\mu_{\mathrm{r},2}$ are both assumed to be unity. At a common transverse cross section A of the two structures at z, which contains areas of nonvanishing fields, the two sets of fields satisfy the following generalized reciprocity theorem in the differential form [35]:

$$\begin{aligned}&\frac{\partial}{\partial z}\int_A \mathrm{d}\boldsymbol{\rho}\,\hat{z}\cdot[\mathbf{E}_1(\mathbf{r})\times\mathbf{H}_2(\mathbf{r})-\mathbf{E}_2(\mathbf{r})\times\mathbf{H}_1(\mathbf{r})]\\ &=-i\omega\varepsilon_0\int_A \mathrm{d}\boldsymbol{\rho}\,[\varepsilon_{\mathrm{r},1}(\mathbf{r},\omega)-\varepsilon_{\mathrm{r},2}(\mathbf{r},\omega)]\,\mathbf{E}_1(\mathbf{r})\cdot\mathbf{E}_2(\mathbf{r})-\int_A \mathrm{d}\boldsymbol{\rho}\,[\mathbf{E}_1(\mathbf{r})\cdot\mathbf{J}_2(\mathbf{r})-\mathbf{E}_2(\mathbf{r})\cdot\mathbf{J}_1(\mathbf{r})]\,.\end{aligned} \tag{3}$$

Later, we will set $[\mathbf{E}_1(\mathbf{r}),\mathbf{H}_1(\mathbf{r})]$ to modal fields of the circular PEC WG with $\mathbf{J}_1(\mathbf{r})=\mathbf{0}$ and $\varepsilon_{\mathrm{r},1}(\mathbf{r},\omega)=\varepsilon_{\mathrm{b}}(\omega),\ \forall\ 0<\rho<R$. The fields $[\mathbf{E}_2(\mathbf{r}),\mathbf{H}_2(\mathbf{r})]$ will be identified as the scattered fields $[\mathbf{E}_{\mathrm{s}}(\mathbf{r}),\mathbf{H}_{\mathrm{s}}(\mathbf{r})]$ generated by $\mathbf{J}_2(\mathbf{r})=\mathbf{J}_{\mathrm{s}}(\mathbf{r})$ in the chiral PhC $[\varepsilon_{\mathrm{r},2}(\mathbf{r},\omega)=\varepsilon_{\mathrm{r,c}}(\mathbf{r},\omega)]$, where $\mathbf{H}_{\mathrm{s}}(\mathbf{r})$ is the magnetic field associated with $\mathbf{E}_{\mathrm{s}}(\mathbf{r})$.

As an application of Eq. (3), we obtain the orthogonality relation for modes in the circular PEC WG. Let us denote the electric and magnetic fields $[\mathbf{E}^{\sigma}_{mns}(\mathbf{r}),\mathbf{H}^{\sigma}_{mns}(\mathbf{r})]$ of these modes as

$$[\mathbf{E}^{\sigma}_{mns}(\mathbf{r}),\mathbf{H}^{\sigma}_{mns}(\mathbf{r})]=[\mathscr{E}^{\sigma}_{mns}(\boldsymbol{\rho}),\mathscr{H}^{\sigma}_{mns}(\boldsymbol{\rho})]\,\frac{e^{im\phi}}{\sqrt{2\pi}}e^{i\sigma\beta_{mns}z}, \tag{4}$$

where s indicates TE/TM types; $\sigma=+1$ and -1 (or "f" and "b") means forward- and backward-propagating/evanescent modes along the z axis, respectively; $\mathscr{E}^{\sigma}_{mns}(\boldsymbol{\rho})$ and $\mathscr{H}^{\sigma}_{mns}(\boldsymbol{\rho})$ are transverse profiles of mode (m,n,s,σ) aside from the azimuthal part $\exp(im\phi)/\sqrt{2\pi}$; and β_{mns} is the associated propagation constant which is identical to $\beta_{-m,ns}$ (degenerate if $m\neq 0$) and is either positive (propagating) or purely imaginary with $\mathrm{Im}[\beta_{mns}]>0$ (evanescent). We then assign two sets of fields in Eq. (3) as follows:

$$[\mathbf{E}_1(\mathbf{r}),\mathbf{H}_1(\mathbf{r})]=[\mathbf{E}^{\sigma}_{mns}(\mathbf{r}),\mathbf{H}^{\sigma}_{mns}(\mathbf{r})],\;\; [\mathbf{E}_2(\mathbf{r}),\mathbf{H}_2(\mathbf{r})]=[\mathbf{E}^{\sigma'}_{m'n's'}(\mathbf{r}),\mathbf{H}^{\sigma'}_{m'n's'}(\mathbf{r})], \tag{5}$$

where (m',n',s',σ') are mode labels for the second set of fields. With $\varepsilon_{\mathrm{r},1}(\mathbf{r},\omega)=\varepsilon_{\mathrm{r},2}(\mathbf{r},\omega)$ and $\mathbf{J}_{1,2}(\mathbf{r},\omega)=\mathbf{0}$, the right-hand side (RHS) of Eq. (3) vanishes. Hence, the left-hand side (LHS) of the same equation, after dropping the factor $\exp[i(\sigma\beta_{mns}+\sigma'\beta_{m'n's'})z]$, has to be zero:

$$i(\sigma\beta_{mns}+\sigma'\beta_{m'n's'})\int_A \mathrm{d}\boldsymbol{\rho}\hat{z}\cdot\left[\mathscr{E}^{\sigma}_{mns}(\boldsymbol{\rho})\times\mathscr{H}^{\sigma'}_{m'n's'}(\boldsymbol{\rho})-\mathscr{E}^{\sigma'}_{m'n's'}(\boldsymbol{\rho})\times\mathscr{H}^{\sigma}_{mns}(\boldsymbol{\rho})\right]\frac{e^{i(m+m')\phi}}{2\pi}=0, \quad (6)$$

where the area A is now the circular cross section of the WG. In Eq. (6), if $\sigma\beta_{mns}+\sigma'\beta_{m'n's'}=0$, the surface integral can be nonzero. This situation occurs only when (i) $\sigma=-\sigma'$ (counter-propagating/evanescent modes), and (ii) $\beta_{mns}=\beta_{m'n's'}$ (degenerate modes). Condition (ii) is further limited to the case $m=-m'$ since the integration of $\exp[i(m+m')\phi]/2\pi$ over ϕ in Eq. (6) brings about a Kronecker delta $\delta_{m+m',0}$. These conditions lead to the following mode orthogonality relation in the circular PEC WG:

$$\begin{aligned}&\int_A \mathrm{d}\boldsymbol{\rho}\hat{z}\cdot\left[\mathscr{E}^{\sigma}_{mns}(\boldsymbol{\rho})\times\mathscr{H}^{\sigma'}_{m'n's'}(\boldsymbol{\rho})-\mathscr{E}^{\sigma'}_{m'n's'}(\boldsymbol{\rho})\times\mathscr{H}^{\sigma}_{mns}(\boldsymbol{\rho})\right]\frac{e^{i(m+m')\phi}}{2\pi}\\ =&\sigma\mathscr{N}_{mns}(\omega)\delta_{m+m',0}\delta_{nn'}\delta_{ss'}\delta_{\sigma+\sigma',0},\end{aligned} \quad (7)$$

where $\mathscr{N}_{mns}(\omega)$ is a (complex) normalization factor which could be set frequency-dependent but must be symmetric with respect to m and $-m$, namely, $\mathscr{N}_{mns}(\omega)=\mathscr{N}_{-m,ns}(\omega)$.

3.3. *Coupled-mode theory*

We utilize Eq. (3) to formulate the coupled-mode theory for scattered fields $\mathbf{E}_{\mathrm{s}}(\mathbf{r})$ and $\mathbf{H}_{\mathrm{s}}(\mathbf{r})$ in the chiral PhC. As mentioned in section 3.2, we may set $[\mathbf{E}_1(\mathbf{r}),\mathbf{H}_1(\mathbf{r})]=[\mathbf{E}^{-\sigma}_{-m,ns}(\mathbf{r}),\mathbf{H}^{-\sigma}_{-m,ns}(\mathbf{r})]$ and $[\mathbf{E}_2(\mathbf{r}),\mathbf{H}_2(\mathbf{r})]=[\mathbf{E}_{\mathrm{s}}(\mathbf{r}),\mathbf{H}_{\mathrm{s}}(\mathbf{r})]$. In this way, Eq. (3) is rewritten as

$$\begin{aligned}&\frac{\partial}{\partial z}\int_A \mathrm{d}\boldsymbol{\rho}\hat{z}\cdot\left[\mathbf{E}^{-\sigma}_{-m,ns}(\mathbf{r})\times\mathbf{H}_{\mathrm{s}}(\mathbf{r})-\mathbf{E}_{\mathrm{s}}(\mathbf{r})\times\mathbf{H}^{-\sigma}_{-m,ns}(\mathbf{r})\right]\\ =&i\omega\varepsilon_0\int_A \mathrm{d}\boldsymbol{\rho}\Delta\varepsilon_{\mathrm{r,c}}(\mathbf{r},\omega)\mathbf{E}^{-\sigma}_{-m,ns}(\mathbf{r})\cdot\mathbf{E}_{\mathrm{s}}(\mathbf{r})-\int_A \mathrm{d}\boldsymbol{\rho}\mathbf{E}^{-\sigma}_{-m,ns}(\mathbf{r})\cdot\mathbf{J}_{\mathrm{s}}(\mathbf{r}),\end{aligned} \quad (8)$$

in which the chiral component $\Delta\varepsilon_{\mathrm{r,c}}(\mathbf{r},\omega)$ of the permittivity profile $\varepsilon_{\mathrm{r,c}}(\mathbf{r},\omega)$ inside the chiral PhC appears at the RHS. This chiral component $\Delta\varepsilon_{\mathrm{r,c}}(\mathbf{r},\omega)$ can be reexpressed as

$$\Delta\varepsilon_{\mathrm{r,c}}(\mathbf{r},\omega)=\Delta\varepsilon_{\mathrm{r,c}}(\rho,\phi-qz,\omega)=\sum_{l=-\infty}^{\infty}\Delta\varepsilon^{(l)}_{\mathrm{r,c}}(\rho,\omega)e^{il(\phi-qz)}, \quad (9)$$

where $q=2\pi/P$ is the reciprocal period of pitch P; and $\Delta\varepsilon^{(l)}_{\mathrm{r,c}}(\rho,\omega)$ is the azimuthal Fourier component of $\Delta\varepsilon_{\mathrm{r,c}}(\mathbf{r},\omega)|_{z=0}$ at order l. The chiral PhC is a RH (LH) structure if the argument $\phi-qz$ ($\phi+qz$) is adopted for $\Delta\varepsilon_{\mathrm{r,c}}(\mathbf{r},\omega)$. Therefore, we use $\phi-qz$ for the structure in Fig. 1.

The scattered fields $\mathbf{E}_{\mathrm{s}}(\mathbf{r})$ and $\mathbf{H}_{\mathrm{s}}(\mathbf{r})$ could be expanded well, though incompletely, with transverse mode profiles in the circular PEC WG:

$$[\mathbf{E}_{\mathrm{s}}(\mathbf{r}),\mathbf{H}_{\mathrm{s}}(\mathbf{r})]\approx\sum_{m'n's'\sigma'}A^{\sigma'}_{m'n's'}(z)\left[\mathscr{E}^{\sigma'}_{m'n's'}(\boldsymbol{\rho}),\mathscr{H}^{\sigma'}_{m'n's'}(\boldsymbol{\rho})\right]\frac{e^{im'\phi}}{\sqrt{2\pi}}, \quad (10)$$

where $A^{\sigma'}_{m'n's'}(z)$ is the z-dependent amplitude of mode (m',n',s',σ'). The amplitude $A^{\sigma'}_{m'n's'}(z)$ contains the characteristics of Bloch modes in the 1D chiral PhC and features of the scatter [source $\mathbf{J}_{\mathrm{s}}(\mathbf{r})$]. We then substitute Eq. (10) into Eq. (8). The surface integral at the LHS of Eq. (8) directly picks up the amplitude $A^{\sigma}_{mns}(z)$ through the orthogonality relation in Eq. (7) and leads to the following differential equation:

$$\frac{\partial A^{\sigma}_{mns}(z)}{\partial z} - i\sigma\beta_{-m,ns}A^{\sigma}_{mns}(z) = -\, i\sigma\omega\varepsilon_0 \sum_{m'n's'\sigma'} e^{-i(m-m')qz}\kappa^{\sigma,\sigma'}_{(mns),(m'n's')}(\omega)A^{\sigma'}_{m'n's'}(z) + \sigma J^{\sigma}_{mns}(z), \tag{11a}$$

$$\kappa^{\sigma,\sigma'}_{(mns),(m'n's')}(\omega) \equiv \int_0^R \mathrm{d}\rho\rho\Delta\varepsilon^{(m-m')}_{\mathrm{r,c}}(\rho,\omega)\frac{\mathscr{E}^{-\sigma}_{-m,ns}(\boldsymbol{\rho})\cdot\mathscr{E}^{\sigma'}_{m'n's'}(\boldsymbol{\rho})}{\mathscr{N}_{-m,ns}(\omega)}, \tag{11b}$$

$$J^{\sigma}_{mns}(z) \equiv \int_A \mathrm{d}\boldsymbol{\rho}\,\frac{e^{-im\phi}}{\sqrt{2\pi}}\frac{\mathscr{E}^{-\sigma}_{-m,ns}(\boldsymbol{\rho})\cdot\mathbf{J}_{\mathrm{s}}(\mathbf{r})}{\mathscr{N}_{-m,ns}(\omega)}, \tag{11c}$$

where $\kappa^{\sigma,\sigma'}_{(mns),(m'n's')}(\omega)$ are the coupling coefficients between various modal amplitudes; $J^{\sigma}_{mns}(z)$ is the projection of the source $\mathbf{J}_{\mathrm{s}}(\mathbf{r})$ to mode (m,n,s,σ); and we have used the integral identity $\int_0^{2\pi}\mathrm{d}\phi\exp[i(l-m+m')\phi]/2\pi = \delta_{l,m-m'}$, $\forall\ l-m+m' \in \mathbb{Z}$, in Eq. (11a).

Equation (11a) could be significantly simplified after some physical approximations. As discussed in section 2, the frequency range of the chiral bandgap is designed such that only the $\mathrm{TE}_{\pm 1,1}$ modes of the original circular PEC WG are not cut off. Therefore, we solely consider the four relevant amplitude-source pairs $[A^{\sigma}_{mns}(z), J^{\sigma}_{mns}(z)]$ related to the fundamental TE modes with $(m,\sigma) = (\pm 1, \mathrm{f/b})$. For simplicity, we abbreviate these four pairs, their associated transverse electric-field profiles, normalization factors, and coupling coefficients as $[A^{\sigma}_{m}(z), J^{\sigma}_{m}(z)]$, $\mathscr{E}^{\sigma}_{m}(\boldsymbol{\rho})$, $\mathscr{N}_m(\omega)$, and $\kappa^{\sigma\sigma'}_{mm'}(\omega)$, respectively, by dropping mode labels $n = 1$ and $s = \mathrm{TE}$. Also, the identical propagation constants of these four modes are simply denoted as $\beta(\omega)$.

Around the frequency range of the chiral bandgap, the propagation constant $\beta(\omega)$ is close to $q = 2\pi/P$. Therefore, the amplitude $A^{\sigma}_{m}(z)$ behaves like the phase factor $\exp(i\sigma qz)$. In views of this behavior, we define a slowly-varying amplitude $\tilde{A}^{\sigma}_{m}(z)$ and its source counterpart $\tilde{J}^{\sigma}_{m}(z)$ in addition to the rapid spatial variation of $\exp(i\sigma qz)$ as

$$[A^{\sigma}_{m}(z), J^{\sigma}_{m}(z)] = e^{i\sigma qz}\left[\tilde{A}^{\sigma}_{m}(z), \sigma\tilde{J}^{\sigma}_{m}(z)\right]. \tag{12}$$

Equation (12) also suggests that the phase difference between two amplitudes $A^{\sigma}_{m}(z)$ and $A^{\sigma'}_{m'}(z)$ is approximately reflected on the factor $\exp[i(\sigma-\sigma')qz]$. Comparing this factor with the counterpart $\exp[-i(m-m')qz]$ at the RHS of Eq. (11a), we match their phase variations and, hence, merely keep the coupling coefficients $\kappa^{\sigma\sigma'}_{mm'}(\omega)$ with $\sigma-\sigma' = -(m-m')$. This simplification is the major concept of the coupled-mode theory.

With the aforementioned approximations, we rewrite Eq. (11a) using the four slowly-varying pairs $[\tilde{A}^{\sigma}_{m}(z), \tilde{J}^{\sigma}_{m}(z)]$ in a 4-by-4 matrix form of differential equations as

$$\begin{gathered}
\frac{\partial}{\partial z}\tilde{\mathbf{A}}(z) = i\mathbf{M}\tilde{\mathbf{A}}(z) + \tilde{\mathbf{J}}(z), \\
\tilde{\mathbf{A}}(z) \equiv \begin{pmatrix} \tilde{A}^{\mathrm{f}}_{+}(z) \\ \tilde{A}^{\mathrm{f}}_{-}(z) \\ \tilde{A}^{\mathrm{b}}_{+}(z) \\ \tilde{A}^{\mathrm{b}}_{-}(z) \end{pmatrix}, \ \tilde{\mathbf{J}}(z) \equiv \begin{pmatrix} \tilde{J}^{\mathrm{f}}_{+}(z) \\ \tilde{J}^{\mathrm{f}}_{-}(z) \\ \tilde{J}^{\mathrm{b}}_{+}(z) \\ \tilde{J}^{\mathrm{b}}_{-}(z) \end{pmatrix}, \ \mathbf{M} = \begin{pmatrix} \Delta\kappa(\omega) & 0 & 0 & 0 \\ 0 & \Delta\kappa(\omega) & -\kappa^{(-2)}(\omega) & 0 \\ 0 & \kappa^{(2)}(\omega) & -\Delta\kappa(\omega) & 0 \\ 0 & 0 & 0 & -\Delta\kappa(\omega) \end{pmatrix}, \\
\Delta\kappa(\omega) = \beta(\omega) - \kappa^{(0)}(\omega) - q, \quad \kappa^{(0)}(\omega) = \kappa^{\sigma\sigma}_{mm}(\omega), \\
\kappa^{(2)}(\omega) = \kappa^{\mathrm{bf}}_{+-}(\omega), \quad \kappa^{(-2)}(\omega) = \kappa^{\mathrm{fb}}_{-+}(\omega),
\end{gathered} \tag{13}$$

where $\tilde{\mathbf{A}}(z)$ and $\tilde{\mathbf{J}}(z)$ are column vectors formed by $\tilde{A}^{\sigma}_{m}(z)$ and $\tilde{J}^{\sigma}_{m}(z)$, respectively; $\mathbf{M}$ is a 4-by-4 propagation matrix; $\Delta\kappa(\omega)$, and $\kappa^{(\pm 2)}(\omega)$ are nonzero matrix elements of $\mathbf{M}$; and $\kappa^{(0)}(\omega)$ is the diagonal coupling coefficient. The parameters $\Delta\kappa(\omega)$ and $\kappa^{(0)}(\omega)$ are both real if $\Delta\varepsilon_{\mathrm{r,c}}(\mathbf{r},\omega)$ is real, and with proper choices of $\mathscr{N}_{\pm}(\omega)$, $\kappa^{(\pm 2)}(\omega)$ can be also set real.

The matrix $\mathbf{M}$ is block diagonal. Only its second and third rows/columns are coupled. The eigenvalues $\lambda_u(\omega)$ ($u = 1$ to 4) of $\mathbf{M}$ can be obtained from its characteristic polynomial and are

$$\lambda_1(\omega) = -\lambda_4(\omega) = \Delta\kappa(\omega), \quad \lambda_2(\omega) = -\lambda_3(\omega) = \sqrt{\Delta\kappa^2(\omega) - \kappa^{(-2)}(\omega)\kappa^{(2)}(\omega)}. \tag{14}$$

In fact, $\lambda_u(\omega)$ ($u = 1$ to 4) are wave numbers of the Bloch modes near the chiral bandgap. Note that amplitudes $\tilde{A}^{\mathrm{f}}_{+}(z)$ and $\tilde{A}^{\mathrm{b}}_{-}(z)$ do not mix with others through matrix $\mathbf{M}$, and they correspond to eigenvalues $\lambda_1(\omega)$ and $\lambda_4(\omega)$, respectively. These two eigenvalues are real, indicating that $\tilde{A}^{\mathrm{f}}_{+}(z)$ and $\tilde{A}^{\mathrm{b}}_{-}(z)$ [or $A^{\mathrm{f}}_{+}(z)$ and $A^{\mathrm{b}}_{-}(z)$] are propagating modes toward the $+\hat{z}$ and $-\hat{z}$ directions, respectively. The mode labels (m,σ) of $\tilde{A}^{\mathrm{f}}_{+}(z)$ and $\tilde{A}^{\mathrm{b}}_{-}(z)$ indicate that they are LHCP-like modes discussed in section 2. The other set of eigenvalues $\lambda_{2,3}(\omega)$ originate from the coupling between amplitudes $\tilde{A}^{\mathrm{b}}_{+}(z)$ and $\tilde{A}^{\mathrm{f}}_{-}(z)$. They are imaginary if $\Delta\kappa^2(\omega) - \kappa^{(-2)}(\omega)\kappa^{(2)}(\omega) < 0$, which signifies the regime of chiral bandgaps. In this case, the eigenvectors corresponding to $\lambda_2(\omega)$ and $\lambda_3(\omega)$ represent the forward- and backward-evanescent modes of the chiral PhC, respectively. Also, the mode labels (m,σ) of amplitudes $\tilde{A}^{\mathrm{f}}_{-}(z)$ and $\tilde{A}^{\mathrm{b}}_{+}(z)$ which constitute these two PhC modes reveal that they are RHCP-like.

In the chiral bandgap, only the LHCP-like modes $A^{\mathrm{f}}_{+}(z)$ and $A^{\mathrm{b}}_{-}(z)$ corresponding to eigenvalues $\lambda_{1,4}(\omega)$ can propagate. Their magnitudes directly determine the amounts of power flows radiated by $\mathbf{J}_{\mathrm{s}}(\mathbf{r})$ in the forward and backward directions. Let us consider a scatter which is present inside the chiral PhC at $z \in [z_{\mathrm{L}}, z_{\mathrm{R}}]$, where z_{L} and z_{R} are the leftmost and rightmost ends of the scatter. The incident field $\mathbf{E}_{\mathrm{i}}(\mathbf{r})$ is assumed to be solely composed of the forward-propagating LHCP-like mode with a propagation constant $q + \lambda_1(\omega) = \beta(\omega) - \kappa^{(0)}(\omega)$:

$$\mathbf{E}_{\mathrm{i}}(\mathbf{r}) = A^{\mathrm{f}}_{+,\mathrm{i}}(z)\mathscr{E}^{\mathrm{f}}_{+}(\boldsymbol{\rho})\frac{e^{i\phi}}{\sqrt{2\pi}}, \quad A^{\mathrm{f}}_{+,\mathrm{i}}(z) = \mathscr{A}^{\mathrm{f}}_{+,\mathrm{i}}e^{i[\beta(\omega)-\kappa^{(0)}(\omega)](z-z_{\mathrm{L}})}, \tag{15}$$

where $\mathscr{A}^{\mathrm{f}}_{+,\mathrm{i}}$ is the amplitude of the incident field; and the reference point is now set at z_{L}. From Eqs. (2b), (11c), and (15), the projected source $J^{\mathrm{b}}_{-}(z)$ corresponding to the backward-propagating LHCP-like mode is

$$J^{\mathrm{b}}_{-}(z) = \frac{-i\omega\varepsilon_0}{\mathscr{N}_{+}(\omega)}\mathscr{A}^{\mathrm{f}}_{+,\mathrm{i}}e^{i[\beta(\omega)-\kappa^{(0)}(\omega)](z-z_{\mathrm{L}})}\int_A \mathrm{d}\boldsymbol{\rho}\,\frac{e^{2i\phi}}{2\pi}\left[\Delta\varepsilon_{\mathrm{r,s}}(\mathbf{r},\omega)\mathscr{E}^{\mathrm{f}}_{+}(\boldsymbol{\rho})\cdot\mathscr{E}^{\mathrm{f}}_{+}(\boldsymbol{\rho})\right]. \tag{16}$$

We may directly solve $A^{\mathrm{b}}_{-}(z)$ in terms of $J^{\mathrm{b}}_{-}(z)$ using their differential equation which is converted from that of $[\tilde{A}^{\mathrm{b}}_{-}(z), \tilde{J}^{\mathrm{b}}_{-}(z)]$ in Eq. (13):

$$\frac{\partial}{\partial z}A^{\mathrm{b}}_{-}(z) + i\left[\beta(\omega) - \kappa^{(0)}(\omega)\right]A^{\mathrm{b}}_{-}(z) = -J^{\mathrm{b}}_{-}(z). \tag{17}$$

With the boundary condition $A^{\mathrm{b}}_{-}(z_{\mathrm{R}}) = 0$, the modal amplitude $A^{\mathrm{b}}_{-}(z)$ at $z \le z_{\mathrm{R}}$ is

$$A^{\mathrm{b}}_{-}(z) = \int_z^{z_{\mathrm{R}}} \mathrm{d}z' e^{i[\beta(\omega)-\kappa^{(0)}(\omega)](z'-z)}J^{\mathrm{b}}_{-}(z'). \tag{18}$$

We then define the reflection coefficient $r(\omega)$ as the ratio between the backward-propagating amplitude $A^{\mathrm{b}}_{-}(z_{\mathrm{L}})$ and incident amplitude $A^{\mathrm{f}}_{+,\mathrm{i}}(z_{\mathrm{L}}) = \mathscr{A}^{\mathrm{f}}_{+,\mathrm{i}}$ to quantify the amount of backscattering. Substituting Eq. (16) into Eq. (18), we express $r(\omega)$ as

$$r(\omega) = \frac{A^{\mathrm{b}}_{-}(z_{\mathrm{L}})}{\mathscr{A}^{\mathrm{f}}_{+,\mathrm{i}}} = \frac{-i\omega\varepsilon_0}{\mathscr{N}_{+}(\omega)}\int_{\Omega_{\mathrm{s}}} \mathrm{d}\mathbf{r}'\,\frac{e^{2i\left\{\phi' + [\beta(\omega)-\kappa^{(0)}(\omega)]z'\right\}}}{2\pi}\left[\Delta\varepsilon_{\mathrm{r,s}}(\mathbf{r}',\omega)\mathscr{E}^{\mathrm{f}}_{+}(\boldsymbol{\rho}')\cdot\mathscr{E}^{\mathrm{f}}_{+}(\boldsymbol{\rho}')\right], \tag{19}$$

where Ω_{s} is the scatter region. From Eq. (19), the backscattering in the chiral PhC depends on a volume integral involving $\Delta\varepsilon_{\mathrm{r,s}}(\mathbf{r},\omega)$. This dependency will be addressed in the next section.

#230637 - $15.00 USD Received 12 Dec 2014; revised 2 Apr 2015; accepted 6 Apr 2015; published 14 Apr 2015

4. Comparison between theory and numerical results

4.1. Criteria for prominent backscattering

The reflection coefficient $r(\omega)$ in Eq. (19) is affected by the interplay between $\Delta\varepsilon_{\mathrm{r,s}}(\mathbf{r},\omega)$ and two factors. The first factor is the phase part $\exp(2i\{\phi'+[\beta(\omega)-\kappa^{(0)}(\omega)]z'\})\approx\exp[2i(\phi'+qz')]$, and the second one is the transverse mode profile $\boldsymbol{\mathscr{E}}^{\mathrm{f}}_{+}(\boldsymbol{\rho}')$.

For the former, the cancelation of $\exp[2i(\phi'+qz')]$ generally enhances the volume integral in Eq. (19) even though the effect is relatively minor for small scatters. In other words, the prominent backscattering would occur if $\Delta\varepsilon_{\mathrm{r,s}}(\mathbf{r}',\omega)\sim\exp[-2i(\phi'+qz')]$ in the frequency range of the chiral bandgap. From the analogy of the chiral component $\Delta\varepsilon_{\mathrm{r,c}}(\mathbf{r},\omega)$ in Eq. (9), we expect an effective scatter to be a LH chiral structure with (i) a pitch P_{s} close to P, and (ii) a significant azimuthal Fourier component of $\Delta\varepsilon_{\mathrm{r,s}}(\mathbf{r}',\omega)$ at the order $l=-2$. Let us further write the permittivity variation $\Delta\varepsilon_{\mathrm{r,s}}(\mathbf{r}',\omega)$ of such a LH chiral scatter as

$$\Delta\varepsilon_{\mathrm{r,s}}(\mathbf{r}',\omega)=U(\mathbf{r}')\sum_{l=-\infty}^{\infty}\Delta\varepsilon^{(l)}_{\mathrm{r,s}}(\rho',\omega)e^{il(\phi'+q_{\mathrm{s}}z')}, \tag{20}$$

where $U(\mathbf{r}')$ is an indicator function which is unity in Ω_{s} but zero elsewhere; and $q_{\mathrm{s}}=2\pi/P_{\mathrm{s}}$. If $\Delta\varepsilon_{\mathrm{r,s}}(\mathbf{r}',\omega)$ has the g-fold rotational symmetry along the z axis (invariant if $\phi'\to\phi'+2\pi/g$), only the components $\Delta\varepsilon^{(l=\tau g)}_{\mathrm{r,s}}(\rho',\omega)$ ($\tau\in\mathbb{Z}$) are present, namely, the components exist only if their orders l are multiples of g. It can be verified that for $g\geq 3$, the component $\Delta\varepsilon^{(-2)}_{\mathrm{r,s}}(\rho',\omega)$ vanishes. Therefore, the prominent backscattering only occurs for proper LH chiral scatters with two-fold or rotationally asymmetric cross sections ($g=1,2$).

For effects of $\boldsymbol{\mathscr{E}}^{\mathrm{f}}_{+}(\boldsymbol{\rho}')$, we consider a small scatter region Ω_{s} with $\rho'-\rho_{\mathrm{s}}\in[-\Delta\rho_{\mathrm{s}}/2,\Delta\rho_{\mathrm{s}}/2]$, where ρ_{s} is the transverse distance of the scatter, and $\Delta\rho_{\mathrm{s}}$ is its range ($\Delta\rho_{\mathrm{s}}/R\ll 1$). The radial and azimuthal components $\mathscr{E}^{\mathrm{f}}_{\pm,\rho}(\rho')$ and $\mathscr{E}^{\mathrm{f}}_{\pm,\phi}(\rho')$ of the fundamental TE mode profiles $\boldsymbol{\mathscr{E}}^{\mathrm{f}}_{\pm}(\boldsymbol{\rho}')$ have radial dependencies as follows (dropped prefactors are set real):

$$\left[\mathscr{E}^{\mathrm{f}}_{\pm,\rho}(\rho'),\ \mathscr{E}^{\mathrm{f}}_{\pm,\phi}(\rho')\right]\sim\left[\frac{J_1(k_{\mathrm{t}}\rho')}{k_{\mathrm{t}}\rho'},\ \pm iJ_1'(k_{\mathrm{t}}\rho')\right], \tag{21}$$

where J_1 and J_1' are Bessel function of the first kind and its derivative at the order 1, respectively; and $k_{\mathrm{t}}\approx 1.84/R$ is the transverse wave number of the fundamental TE modes. We note that $\boldsymbol{\mathscr{E}}^{\mathrm{f}}_{+}(\boldsymbol{\rho}')\cdot\boldsymbol{\mathscr{E}}^{\mathrm{f}}_{+}(\boldsymbol{\rho}')=|\mathscr{E}^{\mathrm{f}}_{+,\rho}(\rho')|^2-|\mathscr{E}^{\mathrm{f}}_{+,\phi}(\rho')|^2\neq|\boldsymbol{\mathscr{E}}^{\mathrm{f}}_{+}(\boldsymbol{\rho}')|^2$ and rewrite $r(\omega)$ in Eq. (19) as

$$\begin{aligned}
r(\omega)&=\cdots\int_{\rho_{\mathrm{s}}-\Delta\rho_{\mathrm{s}}/2}^{\rho_{\mathrm{s}}+\Delta\rho_{\mathrm{s}}/2}\mathrm{d}\rho'\rho'\Delta\varepsilon_{\mathrm{r,s}}(\mathbf{r}',\omega)\left[|\mathscr{E}^{\mathrm{f}}_{+,\rho}(\rho')|^2-|\mathscr{E}^{\mathrm{f}}_{+,\phi}(\rho')|^2\right],\\
&\approx\cdots\rho_{\mathrm{s}}\Delta\rho_{\mathrm{s}}f_{-}(\rho_{\mathrm{s}})\left\langle\Delta\varepsilon_{\mathrm{r,s}}(\mathbf{r}',\omega)\right\rangle_{\rho'=\rho_{\mathrm{s}}},\\
\left\langle\Delta\varepsilon_{\mathrm{r,s}}(\mathbf{r}',\omega)\right\rangle_{\rho'=\rho_{\mathrm{s}}}&=\int_{\rho_{\mathrm{s}}-\Delta\rho_{\mathrm{s}}/2}^{\rho_{\mathrm{s}}+\Delta\rho_{\mathrm{s}}/2}\mathrm{d}\rho'\frac{\Delta\varepsilon_{\mathrm{r,s}}(\mathbf{r}',\omega)}{\Delta\rho_{\mathrm{s}}},\quad f_{\mp}(\rho_{\mathrm{s}})=\left[\frac{J_1(k_{\mathrm{t}}\rho_{\mathrm{s}})}{k_{\mathrm{t}}\rho_{\mathrm{s}}}\right]^2\mp\left[J_1'(k_{\mathrm{t}}\rho_{\mathrm{s}})\right]^2,
\end{aligned} \tag{22}$$

where "$\cdots$" represents details other than the radial integral; $\rho_{\mathrm{s}}\Delta\rho_{\mathrm{s}}$ is the scatter area per unit azimuthal angle at $\rho'=\rho_{\mathrm{s}}$; $\langle\Delta\varepsilon_{\mathrm{r,s}}(\mathbf{r}',\omega)\rangle_{\rho'=\rho_{\mathrm{s}}}$ is an average of $\Delta\varepsilon_{\mathrm{r,s}}(\mathbf{r}',\omega)$ at $\rho'=\rho_{\mathrm{s}}$; $f_{-}(\rho_{\mathrm{s}})$ is a function characterizing the position dependency of small scatters in the chiral PhC; and $f_{+}(\rho_{\mathrm{s}})$ describes the radial dependency of $|\boldsymbol{\mathscr{E}}^{\mathrm{f}}_{+}(\boldsymbol{\rho}')|^2_{\rho'=\rho_{\mathrm{s}}}$.

The two functions $f_{\mp}(\rho_s)$ are depicted in Fig. 3 for comparisons. The function $f_{-}(\rho_s)$ vanishes at $\rho_s=0$ but peaks at $\rho_s\approx 0.81R$, while $f_{+}(\rho_{\mathrm{s}})$ is the largest and smallest at $\rho_s=0$ and R, respectively. The behavior of $f_{-}(\rho_s)$ indicates that the prominent backscattering in the chiral PhC takes place as the scatter is near the rim of the structure, at which the modal intensity is

#230637 - $15.00 USD Received 12 Dec 2014; revised 2 Apr 2015; accepted 6 Apr 2015; published 14 Apr 2015

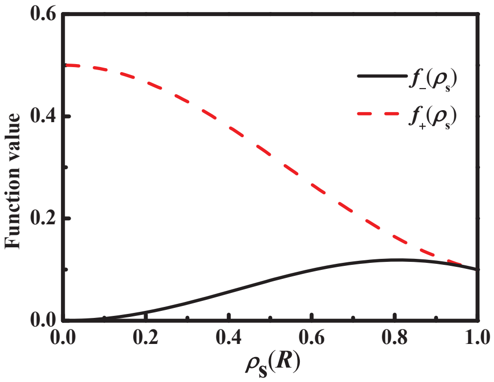

Fig. 3. The two functions $f_\mp(\rho_\mathrm{s})$ versus ρ_s. The function $f_-(\rho_\mathrm{s})$ vanishes at $\rho_\mathrm{s}=0$ but peaks at $\rho_\mathrm{s}\approx 0.81R$, while $f_+(\rho_\mathrm{s})$ is the largest and smallest at $\rho_\mathrm{s}=0$ and R, respectively.

low. The reason for the oddness is that the scattering channels from LHCP-like to RHCP-like modes are suppressed, as the latter become evanescent within the chiral bandgap. If the chirality of the PhC were absent, the backscattered amplitude $A_+^\mathrm{b}(z)$, which is generated by the source $J_+^\mathrm{b}(z)$ and related to an integrand $\Delta\varepsilon_{\mathrm{r,s}}(\mathbf{r}',\omega)\mathscr{E}_-^\mathrm{f}(\boldsymbol{\rho}')\cdot\mathscr{E}_+^\mathrm{f}(\boldsymbol{\rho}')\propto|\mathscr{E}_+^\mathrm{f}(\boldsymbol{\rho}')|^2\propto f_+(\rho')$, could carry power flows. This backscattered amplitude would then show the typical scattering trend of $f_+(\rho_\mathrm{s})$ for the fundamental TE modes in circular PEC WGs.

4.2. Numerical results

With the LHCP-like incident mode of the circular PEC WG at 10.25 GHz, we solve the scattered field inside the chiral PhC using the three-dimensional finite-element method implemented in COMSOL. The two ends of the computation domain are set to perfectly matched layers to make the scattered field an outgoing wave. The power reflectivity $|r(\omega)|^2$ is then obtained from the incident and total fields. Unless otherwise mentioned, there are 32 pitches of chiral structures in the front and backside of scatters. We first consider fictitious chiral scatters with g-fold ($g=1$ to 4) rotationally (a)symmetric cross sections, which are composed of $2g$ identical truncated sectors with permittivity variations alternating in signs [$\Delta\varepsilon_{\mathrm{r,s}}(\mathbf{r},\omega)=\pm\Delta\varepsilon_{\mathrm{r,s}}$]. For conveniences, we will simply call the scatters as g-fold LH/RH scatters hereafter ($g\geq 2$). The radii R_s of these scatters will be varied, but for fair comparisons, their radial widths W_s shall be adjusted accordingly so that the cross-sectional areas A_s remain unaltered.

The cross-sectional geometry of the 2-fold LH scatters as the radius R_s increases is shown in Fig. 4(a) (arrow indicates the handness). The cross-sectional areas are fixed at $A_\mathrm{s}=2\pi R_\mathrm{s}W_\mathrm{s}=0.3\pi R^2$. The pitches P_s and lengths of the scatters are both set to P. The reflectivities $|r(\omega)|^2$ versus R_s at different permittivity variations $\Delta\varepsilon_{\mathrm{r,s}}=0.51$, 0.64, and 0.75 are shown in Fig. 4(b). Although these variations are comparable to the background permittivity $\varepsilon_{\mathrm{r,b}}(\omega)=1$, the trends of $|r(\omega)|^2$ versus R_s qualitatively follow the function $|f_-(R_\mathrm{s})|^2$ in Fig. 3, indicating that the first-order Born approximation and coupled-mode theory work well in these cases. As $R_\mathrm{s}\approx 0.27R$, the scatter cross sections are filled circles and have the best overlap with the most intense portion of the LHCP-like mode. However, the corresponding power reflectivities are minimal. As R_s becomes large, the reflectivities significantly increase. This characteristic indicates that to avoid the prominent backscattering in this chiral PhC, the fluctuations and defects near the rim of the wave-guiding structure should be reduced. On the other hand, the 2-fold RH scatters only backscatter weakly, as shown in Fig. 4(c). They exhibit small power reflectivities that do not seem to have a consistent trend as R_s increases, partly due to the compromise between

Received 12 Dec 2014; revised 2 Apr 2015; accepted 6 Apr 2015; published 14 Apr 2015

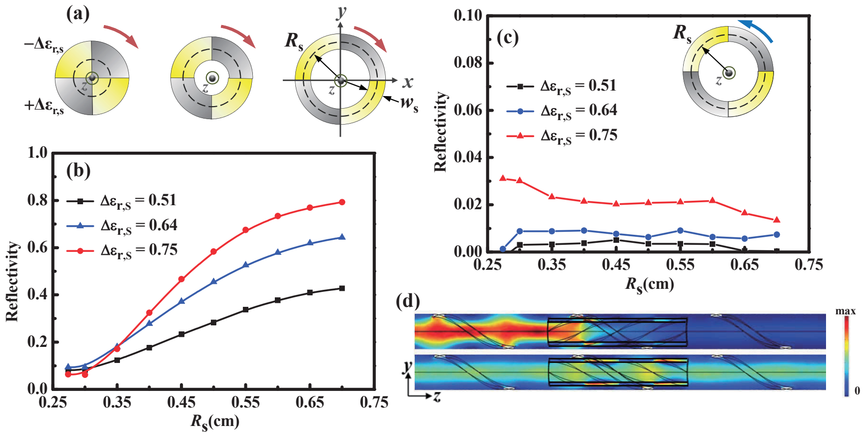

Fig. 4. (a) Cross sections of 2-fold LH scatters as R_s is varied. The cross-sectional areas are fixed at $0.3\pi R^2$. (b) The reflectivities of the 2-fold LH scatters as a function of R_s at various $\Delta\varepsilon_{\mathrm{r,s}}$. The maximal backscattering occurs at the largest R_s in these calculations. (c) The reflectivities of the 2-fold RH scatters as a function of R_s at various $\Delta\varepsilon_{\mathrm{r,s}}$. They are much smaller than their counterparts in (b). (d) The field distributions near the 2-fold LH (top) and RH (bottom) scatters with $R_\mathrm{s} = 0.7R$ and $\Delta\varepsilon_{\mathrm{r,s}} = 0.75$ on the $y-z$ plane, respectively. The incident field is hardly backscattered by the RH scatter.

computational accuracies and dense meshes used in calculations. However, it is certain that the smallness of $|r(\omega)|^2$ originates from the inability of 2-fold RH scatters to compensate the phase factor $\exp(2i\{\phi' + [\beta(\omega) - \kappa^{(0)}(\omega)]z'\})$ in Eq. (19). In Fig. 4(d), we show the field distributions $|\mathbf{E}(\mathbf{r})|^2$ around the 2-fold LH and RH scatters with $R_\mathrm{s} = 0.7R$ and $\Delta\varepsilon_{\mathrm{r,s}} = 0.75$ on the $y-z$ plane. The RH one seems to backscatter little, as can be told from seemingly unaltered magnitudes of the propagating waves at its two sides.

Similar to the 2-fold RH scatter, the 3-fold and 4-fold LH scatters do not backscatter significantly because they only have the azimuthal fourier components at $|l| \geq 3$ and hence cannot compensate the phase factor. The power reflectivities $|r(\omega)|^2$ of these two scatters as a function R_s at different $\Delta\varepsilon_{\mathrm{r,s}}$ are shown in Fig. 5(a) and (b), respectively. The field distributions near the 3-fold and 4-fold LH scatters with $R_\mathrm{s} = 0.3R$ and $\Delta\varepsilon_{\mathrm{r,s}} = 0.75$ are depicted in Fig. 5(c). There are significant local fields confined in the two scatters. However, the local fields mostly correspond to the evanescent modes in the chiral PhC. One can tell that the magnitudes of the propagating waves in the front and backsides of the two scatters remain nearly identical.

The expression of the reflection coefficient $r(\omega)$ in Eq. (22) indicates that the rotationally asymmetric LH scatters ($g = 1$) can also backscatter as long as the azimuthal Fourier component at $l = -2$ is present. From this point, we pick up a group of such scatters exemplified by the inset in Fig. 6(a) intentionally. These LH scatters have no azimuthal Fourier components at $l = -2$ and should not bring about the prominent backscattering in theory. However, their reflectivities at $\Delta\varepsilon_{\mathrm{r,s}} = 0.51$, 0.64, and 0.75 are quite significant, as shown in Fig. 6(a). In addition, the dependencies of the reflectivities on R_s are similar to the function $|f_+(R_\mathrm{s})|^2$. These phenomena mark the breakdown of the first-order Born approximation. We suggest that the failure may be caused by the too large permittivity variation $\Delta\varepsilon_{\mathrm{r,s}}$. As shown in Fig. 6(b), we choose two scatter radii $R_\mathrm{s} = 0.27R$ and $0.7R$ and numerically calculate $|r(\omega)|^2$ as a function of $\Delta\varepsilon_{\mathrm{r,s}}$. Indeed, at $R_\mathrm{s} = 0.27R$, no significant reflections occur at $\Delta\varepsilon_{\mathrm{r,s}} \leq 0.2$, which indicates that the first-order Born approximation is still valid in this regime. The working range of $\Delta\varepsilon_{\mathrm{r,s}}$ for the first-order Born approximation is even larger at $R_\mathrm{s} = 0.7R$. From these observations, we speculate that the

Received 12 Dec 2014; revised 2 Apr 2015; accepted 6 Apr 2015; published 14 Apr 2015

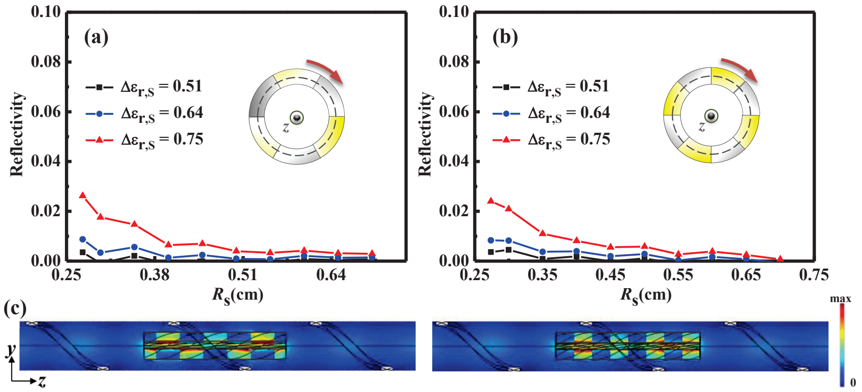

Fig. 5. (a) The reflectivities of the 3-fold LH scatters versus R_s at various $\Delta\varepsilon_{r,s}$, and (b) the counterparts of the 4-fold LH scatters. Both scatters do not backscatter significantly. (c) The field distributions near the 3-fold (left) and 4-fold (right) LH scatters with $R_s = 0.3R$ and $\Delta\varepsilon_{r,s} = 0.75$ on the $y-z$ plane, respectively. Except for the prominent local fields, the magnitudes of the propagating waves change little in these two cases.

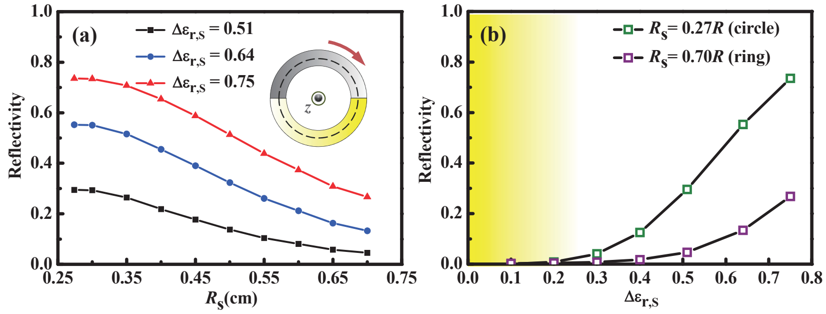

Fig. 6. (a) The reflectivities of the rotationally asymmetric LH scatters versus R_s at various $\Delta\varepsilon_{r,s}$. While the scatters have no azimuthal Fourier components at $l = -2$, the backscattering is prominent. (b) The reflectivities of the rotationally asymmetric LH scatters with $R_s = 0.27R$ and $0.7R$ versus $\Delta\varepsilon_{r,s}$, respectively. The first-order Born approximation breaks down as $\Delta\varepsilon_{r,s}$ becomes too large.

validity of the first-order Born approximation could be quite limited for the chiral scatters with asymmetric cross sections as compared to those with high-order rotational symmetries.

At last, we model the numerical reflection coefficient of a small scatter as a function of its position ρ_s from the center of the chiral PhC using the functional form of $f_-(\rho_s)$. As shown in the inset of Fig. 7, we consider a small copper block with a size of $0.3R \times 0.5R \times 0.3R$ and move it along the direction perpendicular to the line joining the centers of the circular WG and bump. Since the true LHCP-like propagating modes in the chiral PhC slightly deviate from the guiding modes of the circular PEC WG, and the copper block is not infinitesimally small, a finite residual reflection is expected at $\rho_s = 0$ even though the complete transparency is suggested by $f_-(\rho_s = 0)$. Therefore, we approximate the realistic reflection coefficient $r(\omega)$ of the copper scatter with the following form:

$$r(\omega) \approx a f_-(\rho_s) + b, \tag{23}$$

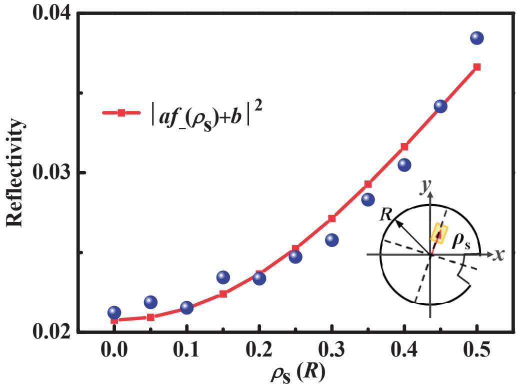

Fig. 7. The reflectivity of a small copper block with a size of $0.3R \times 0.5R \times 0.3R$ versus the position ρ_s. The fitting curve shows a decent agreement with the numerical data.

where a is a proportional factor; and b accounts for the residual reflection. In numerical calculation, only 8 pitches of the chiral structures are placed in the front and backside of the scatter due to the necessary fine meshes around the copper block. The numerical data are then fitted with $|r(\omega)|^2$ based on Eq. (23). As shown in Fig. 7, the fitting curve using Eq. (23) agrees well with the numerical data. The results also indicate that an arbitrary scatter, even if it is not chiral, also backscatters more efficiently as it is farther away from the center of the chiral PhC.

5. Conclusion

We have analyzed the backscattering in a chiral one-way PhC at microwave frequencies. A perturbative method is utilized to obtain criteria for the prominent backscattering. The scattered amplitude depends on the azimuthal Fourier components of scatter cross sections at order $|l| = 2$. Chiral scatters without these Fourier components would not reflect the chiral propagating modes efficiently. This leads to the close dependency of the backscattering on rotational symmetries of chiral scatters. In addition, the disturbance at high-intensity points of the chiral mode does not necessarily lead to the most effective backscattering. Scatters near the rim of the PhC actually backscatter more easily. These characteristics are all qualitatively verified with numerical calculations of the backscattering based on different configurations of scatterers. They also reveal what types of scatters or defects should be avoided in one-way applications of chiral structures in order to minimize the backscattering.

Acknowledgments

This work is sponsored by Research Center for Applied Sciences,Academia Sinica, Taiwan, and Ministry of Science and Technology, Taiwan, under grant number MOST103-2221-E-001-016.

Received 12 Dec 2014; revised 2 Apr 2015; accepted 6 Apr 2015; published 14 Apr 2015